





29 JAMTEC, MGDS, FOCD, and SHOM) on global scale. Generally, NSOAS24(6.33 and 4.95 mGal)  
30 showed comparable accuracy level with DTU21 (6.20 and 4.71 mGal) and SS V32.1 (6.40 and 5.53  
31 mGal), and better accuracy than NSOAS22 (6.64 mGal and 5.64 mGal). Besides, the new model is  
32 available at <https://doi.org/10.5281/zenodo.12730119> (Zhang et al., 2024).  
33



## 34 **1 Introduction**

35 Satellite altimetry provides highly accurate ocean surface height measurements with respect to  
36 certain ellipsoids along corresponding ground tracks (Fu and Cazenave, 2001; Stammer and  
37 Cazenave, 2017). Among these altimetry satellites, some have performed geodetic missions (GM)  
38 with longer revisit period and denser spatial coverage, which provide the primary data sources for  
39 marine gravity recovery. Exact repeat missions (ERM) are also critical in relevant researches  
40 according to a relatively lower noise level by averaging nonunique, repetitive cycles (Zhang et al.,  
41 2022). Due to new altimetry technology and advanced processing methods, the accuracy of sea  
42 surface height (SSH) has increased dramatically over the last decade (Andersen et al., 2023), with  
43 a positive influence on marine gravity model construction. The refinement of altimetry-derived  
44 marine gravity model has become more obvious due to these recent altimetry missions with dense  
45 spatial coverage since 2010, e.g., CryoSat-2, SARAL/AltiKa, Jason-1, Jason-2 and HY-2A GM  
46 (Chen et al., 2024). Combining observations from multiple satellites with different orbital  
47 inclinations such as 108°, 98°, 92°, and 66° enables a more reliable determination of the marine  
48 gravity field (Andersen et al., 2019; Sandwell et al., 2019). In addition to conventional nadir  
49 altimeters, synchronized laser beams for obtaining reflected surface height information, two-  
50 satellite companion mode, and wide-swath altimetry techniques offer new observations and require  
51 effective incorporating strategies for modeling marine gravity field. Furthermore, these  
52 advancements provide new opportunities and potentials for recovering refined marine gravity  
53 anomalies. Generally, combining multi-frequency and multi-mode altimetry data, especially these  
54 observations with higher range accuracy, denser spatial coverage, and diverse track directions, is an  
55 effective way of refining marine gravity recovery (Sandwell et al., 2019).

56 China launched Haiyang-2A (HY-2A) satellite in 2011 and initiated its geodetic mission in  
57 2016 for the purpose of geodetic applications. Multiple previous studies have shown that the HY-  
58 2A has consistent accuracy with other conventional altimetry missions (Wan et al., 2020; Zhang et  
59 al., 2020; Guo et al., 2022b). Moreover, its followers including HY-2B, HY-2C, and HY-2D were  
60 successively launched in 2018, 2020, 2021. Although the HY-2 data cannot serve as the sole input  
61 for constructing a 1'x1' marine gravity anomaly model (Wan et al., 2020; Zhang et al., 2022), the  
62 HY-2 series of measurements are extremely valuable for recovering marine gravity anomalies



63 because of their unique spatial distributions. Currently, several institutions have effectively adopted  
64 HY-2 series data to release regional or global marine gravity models, such as the SCSGA V1.0 (Zhu  
65 et al., 2020), the NSOAS22 (Zhang et al., 2022), the GMGA1 (Wan et al., 2022), the  
66 SDUST2021GRA (Zhu et al., 2022), and the GMGA2 (Hao et al., 2023). Leaving aside the HY-2  
67 series, the most well-known altimetry-derived marine gravity models are DTU and S&S series,  
68 which are respectively released by the Technical University of Denmark and the Scripps Institution  
69 of Oceanography (SIO), University of California San Diego (UCSD). To some extent, they represent  
70 the highest attainable accuracy (Li et al., 2021; Mohamed et al., 2022). Their latest versions have  
71 been updated to DTU21 and S&S V32.1.

72 In a previous study of releasing NSOAS22 model, we primarily evaluated the performance of  
73 HY-2 series altimeter data in constructing marine gravity fields and highlighted the role played by  
74 HY-2. However, we found some obvious issues identified in the NSOAS22 through systematic  
75 evaluation. The first and foremost is the boundary connection problem in block-wise solutions,  
76 which lead to a sawtooth-like discontinuity in the final recovered marine gravity signals. Therefore,  
77 this paper aims to address existing issues and to optimize the model-construction steps for the  
78 purpose of constructing refined marine gravity model. These specific improvements contain dataset  
79 filtering and optimization (supplementing recent observations and removing low-quality data), re-  
80 designing the step sizes for solving DOV with Green's functions, and special processing in near-  
81 shore areas. These improvements will be further described in detail in Section 4.

82 Besides, the remainder of this paper is organized as follows. Section 2 provides a general  
83 description of the involved datasets (altimeter data and shipborne data), as well as the reference  
84 gravity models used for comparison and remove-restore procedure. The theoretical methods for  
85 DOV calculation and gravity anomaly inversion are presented in Section 3. Section 5 evaluates the  
86 altimetry-derived global marine gravity model using the well-known altimetry derived models and  
87 shipborne measurements. Finally, conclusions are given in Section 6, focusing on the 1°x1° global  
88 marine gravity anomaly model named NSOAS24.

## 89 **2 Research data**

### 90 **2.1 Altimetry data**

91 The newly accumulated altimetry data has not only provided high-quality SSH observations



92 but also diverse spatial distributions. For these recent missions, we selected the sensor geophysical  
 93 data records (SGDR), which include high-sampling waveforms from the Jason-1, Jason-2, Jason-3,  
 94 Cryosat-2, HY-2A, HY-2B, and SARAL/AltiKa. In addition, Jason-1, Jason-2, and SARAL/AltiKa  
 95 adopt both ERM and GM data, HY-2A only uses GM data, while HY-2B and Jason-3 only use ERM  
 96 data. Cryosat-2 data comprise three modes: low-resolution mode (LRM), synthetic aperture radar  
 97 (SAR), and synthetic aperture radar interference (SIN). Taking in account the previously collected  
 98 dataset, Geosat observations from both GM and ERM with unique 108° orbital inclination angle,  
 99 along with ERS-1 GM, Envisat and TOPEX/Poseidon ERM datasets, were also utilized. Envisat  
 100 acquired ERM data for two repeated periods, 30 days and 35 days. The detail information of  
 101 involved altimetry data is listed in Table 1.

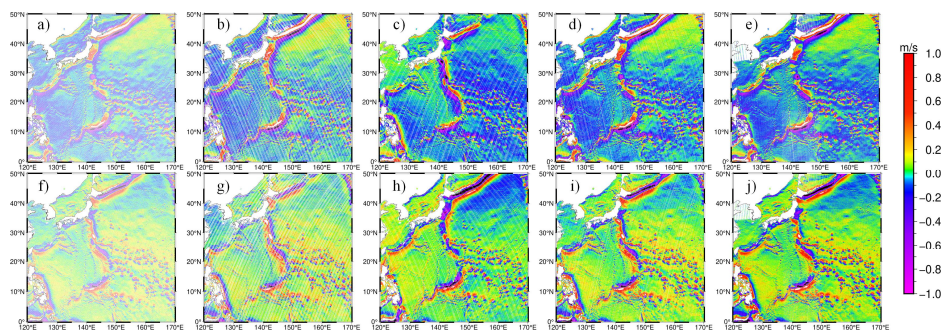
102 **Table 1.** Information of altimetry satellites used for deriving gravity field.

Mission	Satellite	Period	Inclination (°)
Geodetic mission	Jason-1	2012.05-2013.06	66.00
	Jason-2	2017.09-2019.10	66.00
	CryoSat-2	2010.07-2019.04	92.00
	SARAL/AltiKa	2016.07-2024.01	98.55
	HY-2A	2016.03-2019.06	99.30
	Topex/Poseidon	2002.07-2006.10	66.00
	Geosat	1985.04-1986.11	108.10
	ERS-1	1994.4-1995.5	98.52
Exact repeat mission	Jason-1	2008.08-2012.03	66.00
	Jason-2	2008.07-2017.05	66.00
	Jason-3	2016.02-2020.07	66.00
	SARAL/AltiKa	2013.03-2016.07	98.55
	HY-2B	2018.11-2023.11	99.30
	EnviSat	2002.05-2012.04	98.55
	Topex/Poseidon	1992.10-2002.06	66.00
Geosat	1986.12-1990.01	108.10	

103 Along-track SSS can be considered as vector data, and its magnitude is determined by the time  
 104 interval between adjacent ground track points and corresponding SSH variations. Due to different  
 105 design of satellite orbital inclinations and ground track orientations (ascending or descending),  
 106 along-track SSS capture different signal variations and similar signal variation magnitude with  
 107 opposite signs. As shown in Figure 1, satellites with different orbital inclinations exhibit significant



108 differences in along-track slopes obtained in the Mariana Trench area. Ascending and descending  
 109 orbit data both reflect the overall regional trend, exhibiting horizontal symmetry in direction and  
 110 being numerically nearly opposite. For instance, the orbital inclination of HY-2A is approximately  
 111  $99^\circ$ , allowing it to obtain actual data reaching up to around  $81^\circ$  in high-latitude regions. In contrast,  
 112 other altimetry satellites are limited by their designed orbital parameters, such as the Jason series,  
 113 which cannot measure data beyond the  $66^\circ$  region. Satellites with near polar orbit have a data  
 114 coverage advantage in high-latitude regions. Considering the spatial coverage and orientations, the  
 115 calculated slopes should be stored separately based on different orbital inclinations and directions  
 116 to ensure the consistency. Consequently, we categorized these satellites in Table 1 into 5 groups  
 117 based on their orbital design, as shown in Table 2. For multi-cycle data, these are appended to the  
 118 same data file without disrupting temporal continuity, preparing for subsequent segment-based slope  
 119 editing steps.



120  
 121 **Figure 1.** Slope plot of satellite ascent/descent at different orbital inclinations (a, b, c, d, e  
 122 represent ascending track slopes for HY-2A ( $99.3^\circ$ ), Geosat ( $108^\circ$ ), Jason-2 ( $66^\circ$ ), SARAL/AltiKa  
 123 ( $98.55^\circ$ ), CryoSat-2 ( $92^\circ$ ) respectively; f, g, h, i, j represent descending track slopes for HY-2A,  
 124 Geosat, Jason-2, SARAL/AltiKa, CryoSat-2 respectively).

125 **Table 2.** Grouping of satellites according to different orbital inclinations.

i( $108^\circ$ )	ii( $98.55^\circ$ )	iii( $66^\circ$ )	iv( $92^\circ$ )	v( $99.3^\circ$ )
Geosat (GM)	Envisat	TOPEX	CryoSat-2(SAR)	HY-2A(GM)
Geosat (ERM)	Envisat-P	TOPEX-M	CryoSat-2-P(SAR)	HY-2B(ERM)
	SARAL/AltiKa(GM)	Jason-1(GM)	CryoSat-2(SIN)	
	SARAL/AltiKa(ERM)	Jason-1(ERM)	CryoSat-2-P(SIN)	
	SARAL/AltiKa-F	Jason-2(GM)	CryoSat-2(LRM)	
		Jason-2(ERM)		
		Jason-3(ERM)		

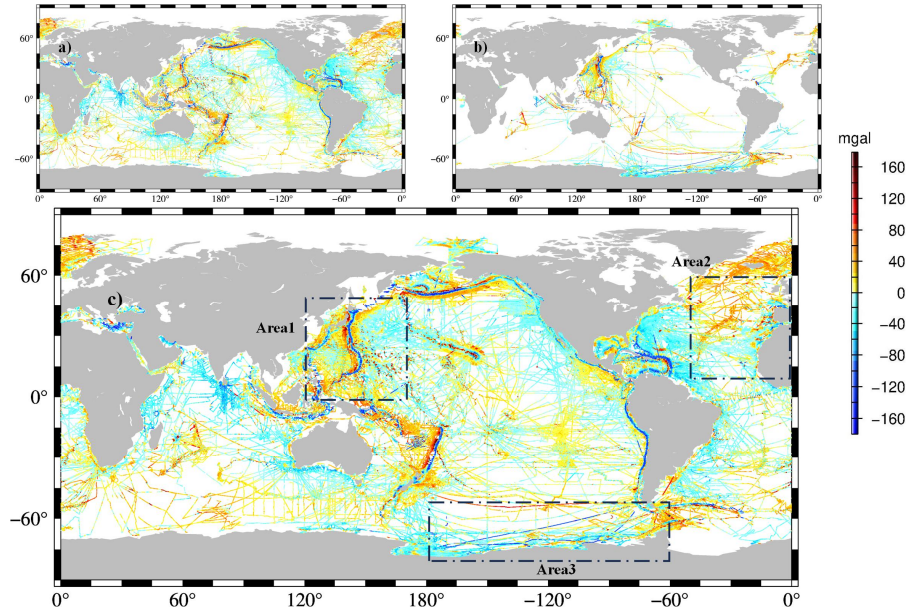


126 **2.2 Typical gravity models**

127 To compare and validate the new global marine gravity model, several well-known models  
128 are introduced. Firstly, the latest version of the S&S series model V32.1, which includes both DOV  
129 and gravity anomaly, is used for comparison and validation purposes, hereinafter referred to as the  
130 V32.1. Secondly, the DTU21 gravity anomaly model is introduced for comparison and validation.  
131 Thirdly, the classical EGM2008 comprehensive series model is introduced, which provides the SSH  
132 along with DOT2008A mean dynamic topography model, DOV, and gravity anomaly (Pavlis et al.,  
133 2012). It serves as the reference model in the remove-restore procedure.

134 **2.3 Shipborne data**

135 Firstly, a total of 10,740,231 ancient shipborne data points were collected from NCEI (National  
136 Centers for Environmental Information). Secondly, a total of 33,522,351 recent measurements from  
137 four marine institutions with relatively high quality were gathered: FOCD (French Oceanographic  
138 Cruises Directory), JAMTEC (Japan Agency for Marine-Earth Science and Technology), MGDS  
139 (Marine Geoscience Data System), and SHOM (French Naval Hydrographic and Oceanographic  
140 Service). The distribution of shipborne data is illustrated in Figure 2. The NCEI data covers global  
141 oceans more comprehensively, whereas non-NCEI data exhibits dense coverage in the nearby  
142 regions of Japan and in the partial Antarctic seas. Due to inevitable outliers in in-situ data, necessary  
143 data editing was conducted using the triple standard deviation criterion by calculating deviations  
144 with respect to the EGM2008 model. As shown in Figure 2(c), three regions, which are marked in  
145 dashed rectangular and span low, mid, and high-latitude oceans (Area1: 0°-50°N, 120°-170°E;  
146 Area2: 10°-60°N, 310°-360°W; Area3: 50°-80°S, 180°-300°W), were selected as experimental  
147 areas.



148  
 149 **Figure 2.** Distribution of shipborne data (a: NCEI; b: FOCD, JAMTEC, MGDS, SHOM;  
 150 c: Total shipborne data, with three experimental areas highlighted in dashed rectangular).

### 151 3. Theoretical methodology

#### 152 3.1 Method of along-track DOV calculation

153 Instead of the derivative of the geoid with respect to the spherical distance, Sandwell et al.  
 154 (1997) proposed a method of calculating along-track DOV with two steps. Firstly, geoid slopes were  
 155 derived from adjacent geoid heights and corresponding temporal variations. Secondly, the along-  
 156 track DOV is computed on basis of geoid slopes by dividing by corresponding satellite orbit  
 157 parameter derived velocity. The procedure is summarized in following formula.

$$158 \quad \varepsilon^{\alpha} = -\frac{\partial N}{\partial s} = -\frac{\partial N}{\partial t} * \frac{\partial t}{\partial s} = -\frac{\partial N}{\partial t} * \frac{1}{v} \quad (1)$$

159 The process for determining the linear velocity  $v$  is as follows. Given a data point's latitude  $\varphi$ ,  
 160 we first convert the geodetic latitude to geocentric latitude  $\varphi_c$  by considering the Earth's flattening  
 161  $e$ . The formula is expressed as follows:

$$162 \quad \varphi_c = \frac{1-e}{\sqrt{\cos^2 \varphi + (1-e)^4 \sin^2 \varphi}} \quad (2)$$

163 Assuming the inclination angle of the satellite's orbit is  $\alpha$ , the period of the orbit's descending  
 164 node is  $T$ , the regression period is  $t$ , the distance between adjacent trajectories is  $s$ , and the





165 equatorial circumference is  $L$ , the average angular velocity  $w_s$  and synchronous Earth velocity  $w_e$   
166 of the satellite's elliptical motion along the orbit can be calculated separately

$$167 \quad w_s = \frac{2\pi}{T} \quad (3)$$

$$168 \quad w_e = \frac{w_s L}{s} \quad (4)$$

169 Subsequently, the angular velocity components  $w_\varphi$  and  $w_\lambda$  along the latitude and longitude  
170 directions can be obtained separately

$$171 \quad w_\varphi = \frac{w_s \cos^2 \varphi}{(1-e)^2 \cos^2 \varphi_c} \sqrt{1 - \frac{\cos^2 \alpha}{\cos^2 \varphi_c}} \quad (5)$$

$$172 \quad w_\lambda = \frac{w_s \cos \varphi}{\cos^2 \varphi_c} - w_e \quad (6)$$

173 Simple synthesis can obtain the angular velocity  $w$  along the orbit

$$174 \quad w = \sqrt{w_\varphi^2 + w_\lambda^2} \quad (7)$$

175 Finally, multiply by the radius of the Earth  $R$  to obtain the ground linear velocity  $v$

$$176 \quad v = wR \quad (8)$$

### 177 3.2 Method of gridded DOV calculation

178 The Green's method proposed by Wessel et al. (1998) restores the along-track DOV to the  
179 gradient direction of the geoid, and subsequently projects it onto the prime (east-west) and  
180 meridional (north-south) components, achieving a similar transformation in the along-track  
181 components (Brammer et al., 1980).

182 For a linear operator  $L$ , the output or response under the action of a point source  $\delta$  is the Green's  
183 function  $G$ ,

$$184 \quad LG = \delta \quad (9)$$

185 where  $L$  is taken as the Laplace operator  $\nabla^2$ ,

$$186 \quad \nabla = i \frac{\partial}{\partial x} + j \frac{\partial}{\partial y} + k \frac{\partial}{\partial z} \quad (10)$$

187 The Green's function formulation transforms to

$$188 \quad \nabla^2 \phi(x) = \delta(x) \quad (11)$$

189 The left-hand side of the above equation represents the product of the Laplace operator and  
190 the Green's function formulation, while the right-hand side corresponds to the Dirac delta function.



191 Solutions that satisfy the Laplace equation are known as harmonic functions, corresponding to cases  
192 where the divergence is zero. The formulation for biharmonic functions is introduced as follows:

$$193 \quad \nabla^4 \phi(x) = \delta(x) \quad (12)$$

194 Splines interpolation, whether in one or two dimensions, corresponds physically to enforcing  
195 a thin elastic beam or plate to conform to data constraints. The same interpolation principles apply  
196 to the two-dimensional Green's function formulation as follows:

$$197 \quad D\nabla^4 \phi(x) - T\nabla^2 \phi(x) = \delta(x) \quad (13)$$

198 In the equation,  $D$  represents stiffness, and  $T$  denotes tension factor.

199 In the discrete case, the following equation holds when there are  $M$  reference points within  
200 the region:

$$201 \quad D\nabla^4 w(x) - T\nabla^2 w(x) = \sum_{j=1}^M c_j \delta(x - x_j) \quad (14)$$

202 Wessel et al. (1998) derived the solution  $w(x)$  through Fourier transformation as:

$$203 \quad w(x) = \sum_{j=1}^M c_j \phi(x - x_j) \quad (15)$$

$$204 \quad \phi(x) = K_0(p|x|) + \log(p|x|) \quad (16)$$

205 When there are  $N$  known points within the region, the following equation matrix can be  
206 constructed:

$$207 \quad w_i = \sum_{j=1}^M c_j \phi(x_i - x_j) \quad i = 1, N \quad (17)$$

208 Thus,

$$209 \quad \mathbf{w} = \mathbf{G}\mathbf{c} \quad (18)$$

210 The along-track DOV is the projection of the gradient of the geoid along the track direction.  
211 The inverse solution is obtained using the Green's function method, simultaneously applying tension  
212 spline functions to ensure curve smoothness. The fundamental concept is to simulate the geoid field  
213 using a finite number of control points. This approach aims to interpolate and recover the DOV at  
214 all grid points. In discrete conditions, the Green's method formula is shown as equation (14), where  
215 the left-hand side represents selected control points and the right-hand side consists of other known  
216 points with radial basis functions. By iteratively solving from the known points towards the control  
217 points, the radial basis coefficients  $c_j$  are determined. This process can be viewed as constructing  
218 the geoid field  $\phi$  using finite elements.

219 Considering that  $\phi(x)$  and  $w_i$  are scalar fields representing the geoid and their corresponding



220 geoid heights, and the actual input data represents the directional derivatives of the geoid,  
221 specifically the along-track DOV vector information. Therefore, introducing the gradient field  
222  $grad\phi(x)$  is formulated as follows in equation (19):

$$223 \quad \nabla\phi(x) = i \frac{\partial\phi}{\partial x} + j \frac{\partial\phi}{\partial y} + k \frac{\partial\phi}{\partial z} \quad (19)$$

$$224 \quad s_i = (\nabla w \cdot n)_i = \sum_{j=1}^M c_j \nabla\phi(x_i - x_j) \cdot n_i \quad i = 1, N \quad (20)$$

$$225 \quad \mathbf{D} = \sum_{j=1}^M c_j \nabla\phi(x_i - x_j) \quad i = 1, N \quad (21)$$

226 When simultaneously taking the directional derivative in the satellite operation direction  $n_i$  on  
227 both sides,  $s_i$  represents the along-track DOV vector.  $\nabla\phi(x)$  corresponds to the gradient field of the  
228 geoid. Considering the varying quality of data from different satellites, uncertainties  $sig$  are  
229 incrementally added to control data quality. Therefore, an equation matrix can be constructed at  
230 reference points:

$$231 \quad \begin{bmatrix} s_1/sig_1 \\ \vdots \\ s_n/sig_n \end{bmatrix} = \begin{bmatrix} c_1 \\ \vdots \\ c_m \end{bmatrix}^T \begin{pmatrix} 0 & \cdots & D_{x_1-x_m} n_1/sig_1 \\ \vdots & \ddots & \vdots \\ D_{x_n-x_1} n_n/sig_n & \cdots & 0 \end{pmatrix}^T \quad i = 1, N \quad j = 1, M \quad (22)$$

232 After solving for the coefficients  $c_j$ , the construction of the geoid gradient field is completed.  
233 At any grid point, the geoid gradient  $\mathbf{D}$  can be determined. Multiplying this gradient by the east-  
234 west and north-south directional vectors yields the DOV components at each grid point.

235 The Green's function method offers several advantages. Firstly, it innovatively applies  
236 directional gradients rather than SSH to constrain the model surface, in order to enhance stability.  
237 Secondly, it employs least squares fitting instead of exact interpolation, effectively mitigating the  
238 impact of noisy data points. Additionally, by incorporating tension constraints, it facilitates data  
239 smoothing. For moderate data volumes, the Green's function method is superior to traditional finite  
240 difference methods. However, Green's functions also present certain limitations, such as their  
241 inability to handle excessively large datasets, challenges with boundary discontinuities, and  
242 suboptimal performance in near-shore areas. These issues will be discussed and addressed in Section  
243 4.

### 244 3.3 Method of deriving gravity anomalies

245 The relationship between DOV and gravity disturbances or anomalies can be deduced by the  
246 Laplace equation (Sandwell and Smith 1997). The relationships are established according to the



247 internal connections among the disturbing potential  $T$ , gravity disturbances  $\delta g$ , gravity anomaly  
248  $\Delta g$ , and two directional components of DOV ( $\xi$  and  $\eta$ ). Assuming a flat Earth approximation, the  
249 disturbing potential  $T$  satisfies the Laplace equation in the given local planar coordinate system ( $x$ ,  
250  $y$ ,  $z$ ). Then, the relationship between gravity and DOV can be established as the following equation.

$$251 \quad \frac{\partial \delta g}{\partial z} = -\gamma_0 \left( \frac{\partial \xi}{\partial x} + \frac{\partial \eta}{\partial y} \right) \quad (23)$$

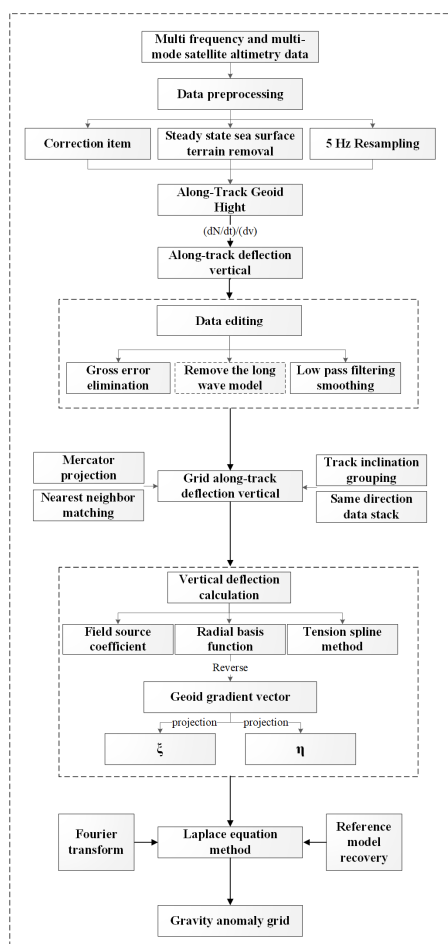
252 Taking the difference between gravity disturbance and gravity anomaly into account, the gravity  
253 anomaly is further calculated according to,

$$254 \quad \Delta g(x, y) = \delta g(x, y) - \frac{2\gamma_0}{R} N(x, y) \quad (24)$$

255 where  $R$  is the average radius of Earth, and  $N$  is the geoid height, which can be provided by geo-  
256 potential models. For the detailed computation procedure, please refer to Zhang et al. (2020).

#### 257 **4 Model construction**

258 Based on the theories summarized in Section 3, we sequentially calculated along-track SSH,  
259 SSS, along-track DOV, gridded DOV and gridded gravity anomalies from multi-frequency and  
260 multi-mode satellite altimetry data. For the purpose of model construction, a series of joint  
261 processing strategies, e.g., waveform retracking, adding corrections, resampling, data editing,  
262 filtering, as well as the remove-and-restore procedure were necessary. The specific construction  
263 steps are illustrated in Figure 3.



264

265

**Figure 3.** Flowchart of constructing marine gravity model from multi-satellite altimeter data.

266

#### 4.1 Data preprocessing and slope editing

267

Firstly, raw waveforms were retracked using the two-step weighted least-square retracker

268

(Zhang and Sandwell, 2017), and high-rate observations along profiles were uniformly resampled

269

into 5 Hz to constrain the noise level and enhance the density of available measurements. Secondly,

270

along-track SSH measurements were calculated by adding correction items provided in the SDR

271

products to amend corresponding effects for path delay and geophysical environment. Then the

272

along-track slopes were calculated, and their accuracy was validated with the EGM2008 model

273

slopes. If the deviations exceed the setting threshold according to the triple standard deviation

274

criterion, the data point is considered unreliable and removed. If excessive data segments are edited

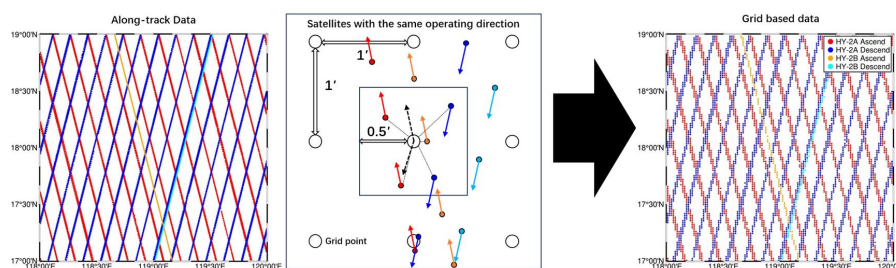


275 out, the entire segment is abandoned to prevent the influence of outliers on subsequent calculations.  
276 Finally, a Parks–McClellan filter was adopted for all these slopes to constrain the amplified high-  
277 frequency noise during the difference procedure.

#### 278 **4.2 Gridding along-track DOV**

279 Firstly, along-track velocities corresponding to different satellites were calculated to convert  
280 along-track slopes to along-track DOV. Then along-track residual DOVs were computed by filtering  
281 the EGM2008 geoid heights and corresponding DOT2008A\_n180 sea surface topography. Before  
282 gridding, it is necessary to define the objective grid in advance. Considering that the inversion grid  
283 should closely resemble the real earth, a Mercator projection grid was chosen in this study. The  
284 Mercator projection is a cylindrical map projection that preserves angles and is used for a 1'×1'  
285 global grid, with 21,600 grid points in both latitude and longitude directions (The latitude direction  
286 uses the Gudermannian function transformation, while the longitude direction is uniformly divided).  
287 After defining the gridding points, along-track slopes were gridded using a nearest-neighbor  
288 approach. Satellites are categorized based on orbital inclination and ground track orientation, which  
289 ensures that the along-track DOV direction remains consistent and averages potentially redundant  
290 data points in the same direction at grid points, thereby reducing data complexity. Due to the  
291 requirements of the Green's function method regarding region size and data volume, convergence  
292 of multiple vectors with different values at same gridding points with consistent direction can render  
293 the matrix singular. By the way, the averaging step between each category was essential to address  
294 this issue.

295 As mentioned above, along-track DOVs were mapped to gridding points. Taking the HY-2  
296 group for instance, the gridding process for ascending and descending track segments is illustrated  
297 in Figure 4. Matching is performed using the nearest-neighbor method, and data stacking follows  
298 the principle of consolidating data in the same direction. The specific process is summarized as  
299 follows. (1) Determine the number and position of 1'×1' grid points implemented using the Mercator  
300 projection. (2) Project the geodetic latitude and longitude of input data to Mercator coordinates, and  
301 determine the nearest grid point in the Mercator coordinate system for each data point. (3) Perform  
302 weighted averaging for data in the same direction, and store data from different groups separately.



303

304

**Figure 4.** Gridding along-track DOVs at grid points (HY-2 group for example)

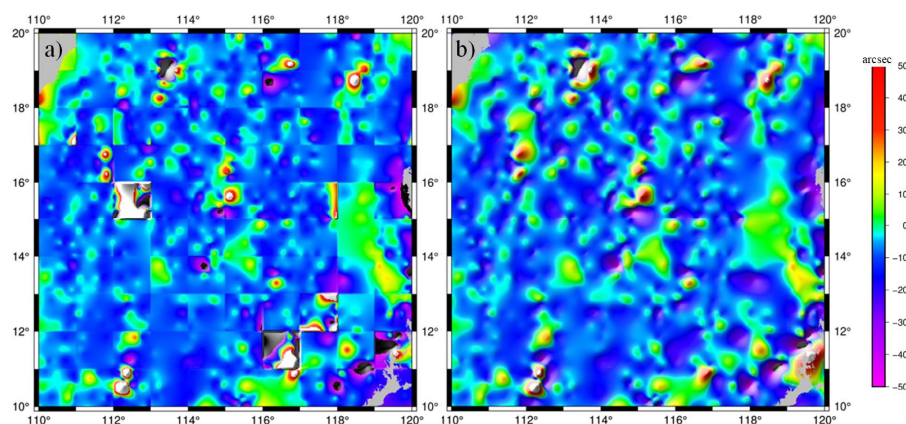
305

### 4.3 DOV components calculation

306

Limited by the computing power of computer and massive gridding points, the DOV components were calculated with block-wise input and output to avoid excessive computational redundancy and matrix singularity. While constructing NSOAS22 model, the tension spline method overlooked the impact of coherence between block-wise regions. This tension spline interpolation is typically suitable for solving small to moderate-sized regions with medium data volumes. However, excessive data can drastically reduce computational efficiency and potentially cause stack overflow issues. Consequently, constraints arising from the distribution of known points may lead to ineffective solving at boundaries and discontinuities between adjacent regions, as illustrated in Figure 5(a). In this study, we proposed a new solution by enlarging computation regions while restricting output to central areas to ensure continuity. Specifically, the inputs were chosen within a 64\*64 grid, and the outputs were exclusively limited to the central 32\*32 grid. As illustrated in Figure 5(b), the discontinuous effect was eliminated.

317



318

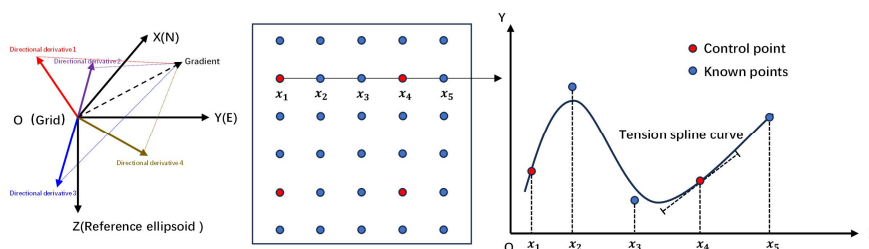
319

**Figure 5.** Result of spline splicing method for DOV east-west components (a: original; b: new)



320 **4.3.1 Step selection**

321 To compute DOV components using the Green's function method, it is necessary to select  
 322 specific grids as control points for iterative processes. The graphical representation of solving DOV  
 323 components using the Green's function method is illustrated in Figure 6. Additionally, the tension  
 324 spline interpolation demonstrates optimal performance when control points are evenly distributed.  
 325 Leveraging the regularity of the grid, the step size (interval between two control points) is defined  
 326 for selecting control points. An increased number of control points tends to render the spline curve  
 327 more rigid, thereby accentuating large fluctuations and noise. Conversely, a reduced number of  
 328 control points leads to a sparser spline curve that appears smoother, effectively mitigating noise.  
 329 However, sparse control points may result in an overly simplistic representation of the field. As  
 330 control points become sparser, the interpolation distance increases, thereby reducing the reliability  
 331 of the results.



332

333

**Figure 6.** Green's function method for solving DOV components

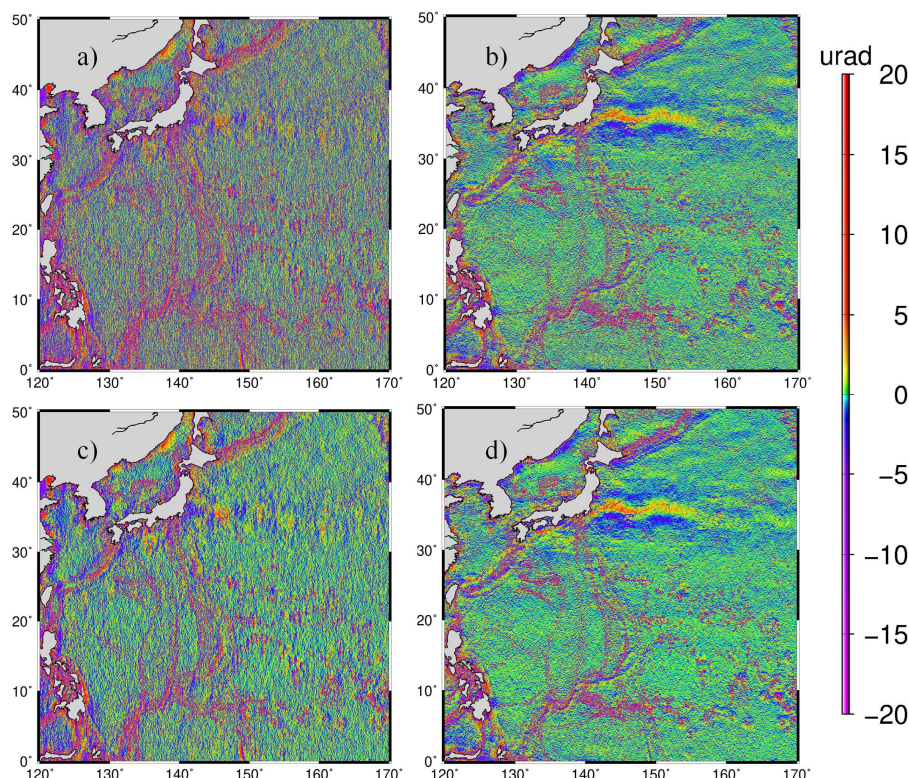
334

335 Our computational grid size is 64\*64, offering different control point densities based on step  
 336 sizes: 4096 control points with step size 1, 1024 with step size 2, and 441 with step size 3. Larger  
 337 step sizes lead to fewer control points, which may not adequately represent the region. Step size 1  
 338 results in excessive noise, affecting signal continuity and computational efficiency. Hence, step sizes  
 339 2 and 3 are under consideration in our study for balancing detail and computational feasibility.

339

340 In experimental area 1 in Figure 2(c), the residual DOV for step sizes 2 and 3 is shown in  
 341 Figure 7. The figure demonstrates that with a step size of 2, noticeable noise artifacts are introduced,  
 342 particularly impacting the east-west components. In contrast, using a step size of 3 results in  
 343 smoother outcomes, exhibiting clearer distribution characteristics of the DOV components. The  
 reduction of noise is particularly effective in specific areas like near-shore regions and islands.





344

345

346 **Figure 7.** Residual results of DOV components difference for different step size selections (a:  
347 east-west component at 2 steps; b: north-south component at 2 steps; c: east-west component at 3  
348 steps; d: north-south component at 3 steps)

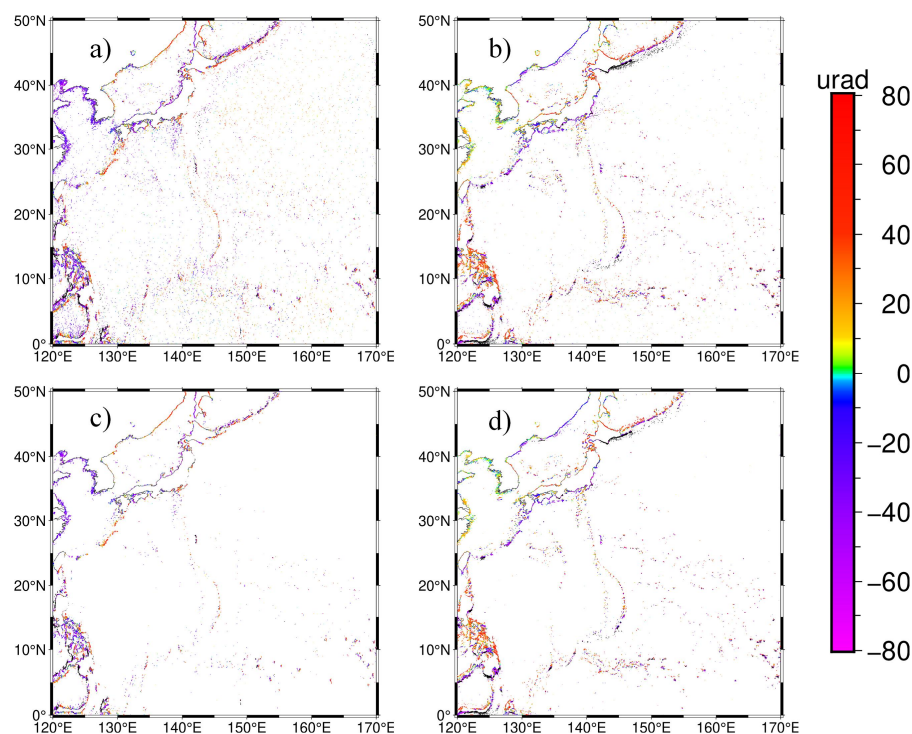
349

350 Then we analyzed the distribution of noise under different step sizes. The V32.1 serves as an  
351 verification model, against which the DOV results obtained with a step size of 2 are subtracted. The  
352 standard deviation is  $3.19 \mu\text{rad}$  for the east-west component and  $2.02 \mu\text{rad}$  for the north-south  
353 component. Setting a threshold based on the triple standard deviation criterion, the primary noise  
354 locations are depicted in Figure 8(a) and (b). There are 125,456 noise points in the east-west  
355 component, accounting for 1.20% of the entire region, and 122,976 noise points in the north-south  
356 component, making up 1.19% of the total area. After removing these noise points, the standard  
357 deviations reduce to  $2.45 \mu\text{rad}$  for the east-west component and  $1.36 \mu\text{rad}$  for the north-south  
358 component. With a step size of 3, the standard deviations are respectively  $2.37 \mu\text{rad}$  for the east-  
359 west component and  $1.75 \mu\text{rad}$  for the north-south component. Identifying based on the triple  
standard deviation criterion, the primary noise locations are shown in Figure 8(c) and (d). There are



360 77,904 noise points in the east-west component, accounting for 0.75% of the entire region, and  
361 105,923 noise points in the north-south component, comprising 1.02% of the total area. After  
362 removing outliers, the standard deviations decrease to 1.84  $\mu\text{rad}$  for the east-west component and  
363 1.20  $\mu\text{rad}$  for the north-south component.

364 It is evident that the noise in the east-west component is noticeably reduced with a step size of  
365 3 compared to that with a step size of 2. Moreover, scattered noise points in open ocean areas are  
366 massively eliminated. This is to say, the selection of step size significantly influences both the  
367 distribution and magnitude of noise points. Considering on larger step size's advantages in enhanced  
368 computational efficiency, reduced matrix complexity, and lower mitigate noise, we finally selected  
369 step size 3 for acquiring controlling points.



370  
371 **Figure 8.** Noise analysis at different step sizes (a: east-west component at step size 2; b:  
372 north-south component at step size 2; c: east-west component at step size 3; d: north-south  
373 component at step size 3)

374 In addition, comparisons between step sizes were conducted in two other experimental areas,  
375 and the statistical results are presented in Table 3. It's interesting that Experimental area 3 exhibits  
376 distinctive characteristics. Satellites with lower inclinations, such as the Topex/Poseidon and Jason



377 series, are unable to provide observations beyond 66°, resulting in a noticeable decline in DOV  
 378 quality in high-latitude regions.

379 **Table 3.** Statistics of DOV components with respect to V32.1 for different step sizes (unit:  $\mu\text{rad}$ )

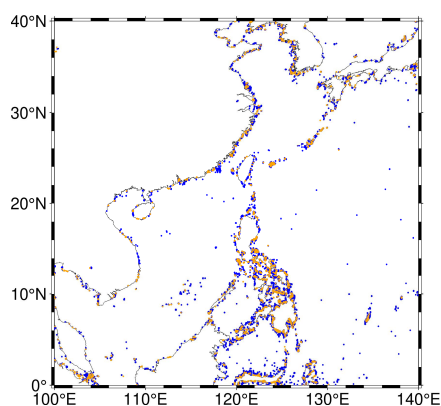
Area	Step size	DOV components	Max	Min	Mean	STD
1	2	East-west	623.07	-610.62	-0.02	3.19
	3	East-west	258.74	-393.84	-0.02	2.37
	2	North-south	613.82	-614.79	0.01	2.02
	3	North-south	388.40	-401.70	0.01	1.75
2	2	East-west	326.62	-327.40	-0.03	2.40
	3	East-west	628.80	-286.61	-0.03	1.80
	2	North-south	327.37	-328.91	0.00	1.50
	3	North-south	400.27	-584.03	0.00	1.39
3	2	East-west	634.40	-639.41	0.11	5.41
	3	East-west	518.80	-644.39	0.09	4.34
	2	North-south	636.89	-634.96	-0.09	4.61
	3	North-south	620.09	-522.40	-0.10	3.74

380 **4.3.2 Special processing in near-shore areas**

381 Along the coastline, SSH measurements are typically available only on the ocean side, while  
 382 grid points over land are default values and posing computational challenges. As illustrated in Figure  
 383 8, increasing the step size effectively reduced a considerable number of noise points over the open  
 384 sea, while the remaining noise points majorly concentrated in near-shore areas. To demonstrate the  
 385 effect of special processing in near-shore areas, we chose the China sea and its adjacent waters  
 386 ( $100^{\circ}$ - $140^{\circ}$ E,  $0^{\circ}$ - $40^{\circ}$ N) as the experimental area. This area is densely distributed with islands and  
 387 reefs, involving typical categories of coastal regions. Based on the calculated residual DOV with  
 388 respect to V32.1, we distinguished noise points where the absolute deviation exceeds 20  $\mu\text{rad}$ . The  
 389 distribution of noise points near the coastlines is more pronounced, as shown in Figure 9. The east-  
 390 west component and north-south component noise points account for 0.27% and 0.09% of the total  
 391 grid points in the region, respectively. It is evident that larger noise points are more prevalent in the  
 392 anomalous computation of the east-west component. Therefore, special treatment is required in  
 393 near-shore areas to mitigate the concentrated occurrence of noise. As previously mentioned, the  
 394 Green's function method operates within a  $64*64$  grid area. When handling near-shore regions, the  
 395 grids over land lack data, with controlling points only available on the ocean side. Thus, the actual  
 396 data boundary is at the coastline, but not at the edges of the  $64*64$  grid. These mixed zones directly  
 397 cause boundary effects that hinder matrix convergence. Expanding the computation area is not a  
 398 feasible solution because even with an enlarged area, there are no effective data points over land to



399 provide constraints. Solutions without constraints typically exhibit lower reliability, contributing  
400 significantly to the observed noise in coastal areas. Figure 10 further gives these differences between  
401 calculation and V32.1 over land-influenced 64\*64 grid areas, showing the approximate outline of  
402 the block-wise rectangular computational regions in finer detail. The influential grid points in near-  
403 shore areas account for 10% of the total grid points. Additionally, there are 30% of grid points over  
404 land within the influential region, indicating a significant proportion of near-shore grid points.

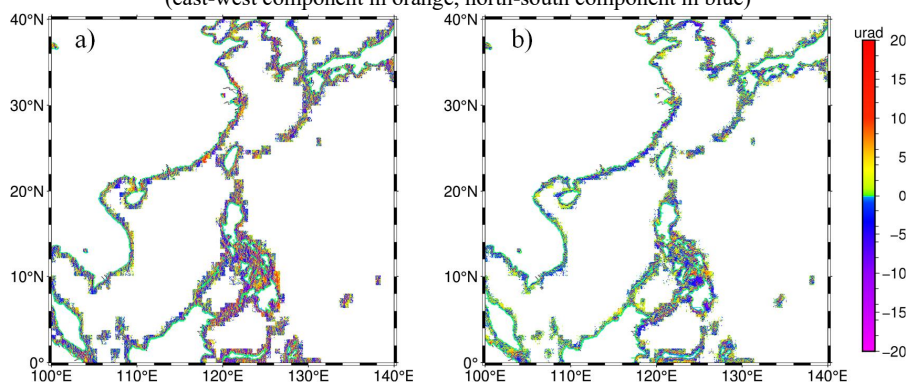


405

406

407

**Figure 9.** The main locations of noise distribution in the near-shore area  
(east-west component in orange, north-south component in blue)



408

409

410

**Figure 10.** Location of distribution of nearshore areas disturbed by continental regions  
(a: east-west component; b: north-south component)

411

412

413

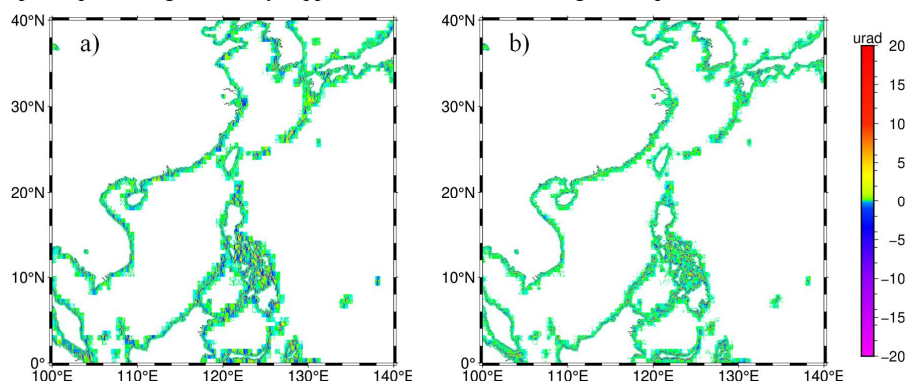
414

415

To constrain this boundary effect, special processing steps were implemented. A continental mask was applied to identify controlling points over land, which were assigned a value of 0 and treated as known points. Moreover, these points were assigned relatively huge uncertainties to minimize their weight. This approach effectively mitigated boundary effects, thereby controlling data divergence and improving the reliability of computations in these land-influenced regions.



416 Figure 11 illustrates the difference in nearshore points before and after processing. Following the  
 417 adjustments, there is almost no change on the seaward side. Whereas on the landward side, the  
 418 standard deviation shows a difference of  $1.67 \mu\text{rad}$  in the east-west component and  $1.47 \mu\text{rad}$  in the  
 419 north-south component, with a maximum difference of around  $60 \mu\text{rad}$ . This indicates that this  
 420 special processing effectively suppressed the occurrence of large noise points near the coastlines.



421 **Figure 11.** Difference in results in the nearshore area before and after the special processing  
 422 (a: east-west component; b: north-south component)

423  
 424 Statistical analysis was also conducted in three experimental areas, and the results are listed in  
 425 Table 4. The first and foremost is that the nearshore constraint effectively reduced the magnitude of  
 426 maximum and minimum deviations. Especially in areas 1 and 2, maximum and minimum values  
 427 were notably declined, indicating an effective constraint on the occurrence of large noise spikes.  
 428 Moreover, similarly using a deviation threshold of  $20 \mu\text{rad}$  for identifying noise points, the overall  
 429 noise ratios decreased by 17.6% following this optimization effort.

430 **Table 4.** Statistics on the difference with respect to V32.1 with or without nearshore constraint  
 431 (unit:  $\mu\text{rad}$ )

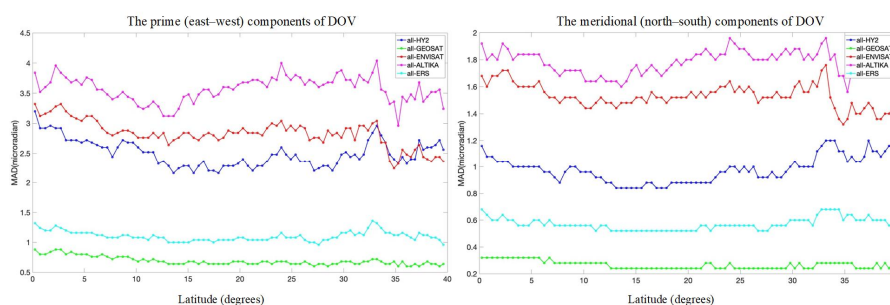
Area	Near-shore constraints	DOV components	Max	Min	Mean	STD
1	Yes	East-west	110.52	-96.43	-0.03	2.42
	No	East-west	258.74	-393.84	-0.02	2.37
	Yes	North-south	68.41	-87.66	0.02	1.76
	No	North-south	388.40	-401.70	0.01	1.75
2	Yes	East-west	95.22	-75.06	-0.03	1.77
	No	East-west	628.80	-286.61	-0.03	1.80
	Yes	North-south	81.95	-70.86	0.01	1.28
	No	North-south	400.27	-584.03	0.00	1.39
3	Yes	East-west	447.94	-644.39	0.09	4.35
	No	East-west	518.80	-644.39	0.09	4.34
	Yes	North-south	620.09	-461.79	-0.10	3.81
	No	North-south	620.09	-522.40	-0.10	3.74





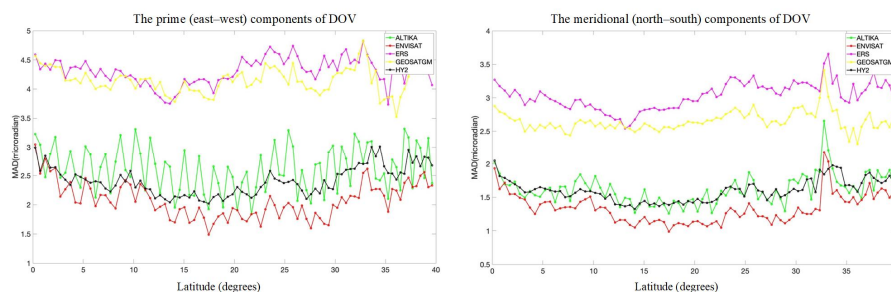
432 **4.3.3 Remove ERS-1 data**

433 To evaluate the contribution of each individual mission to multi-satellite altimetry derived DOV,  
 434 each satellite (SARAL/AltiKa, EnviSat, HY-2A/B, Geosat, and ERS-1) was sequentially removed  
 435 within the China sea and its adjacent waters (100°-140°E, 0°-40°N). Median Absolute Deviations  
 436 (MAD) of the east-west and north-south components along latitude were computed, with the  
 437 NSOAS24 DOV without data removal used as a comparison. Land-influenced zero values were  
 438 excluded during this experiment. The results were presented in Figure 12, which illustrates that  
 439 SARAL/AltiKa provides the most reliable data and the largest contribution. HY-2 also significantly  
 440 influences the DOV, resulting in discrepancies exceeding 2.5  $\mu\text{rad}$  in the east-west component and  
 441 ranging from 1 to 1.5  $\mu\text{rad}$  in the north-south component. ERS-1 and Geosat have a relatively minor  
 442 contribution, causing differences of less than 1.5  $\mu\text{rad}$  and 1  $\mu\text{rad}$  respectively in the east-west and  
 443 north-south components. This also suggests that their signals overlap to a greater extent with other  
 444 satellites.



445 **Figure 12.** Difference in median absolute deviations between NSOAS24 DOV and DOV in the  
 446 absence of certain mission (The greater the difference, the larger the influence).  
 447

448 Additionally, DOV components were calculated for several single satellite mission, and the  
 449 MAD between them and V32.1 in latitude direction was compared. As shown in Figure 13, the  
 450 MAD values are consistently small for HY-2, ENVISAT, and SARAL/AltiKa. However, the data  
 451 from Geosat and ERS-1 exhibit significant deviations, suggesting considerably higher noise levels.



452

453 **Figure 13.** Difference in median absolute deviations between V32.1 DOV and the single satellite  
454 solution (The smaller the difference, the better the DOV solution).

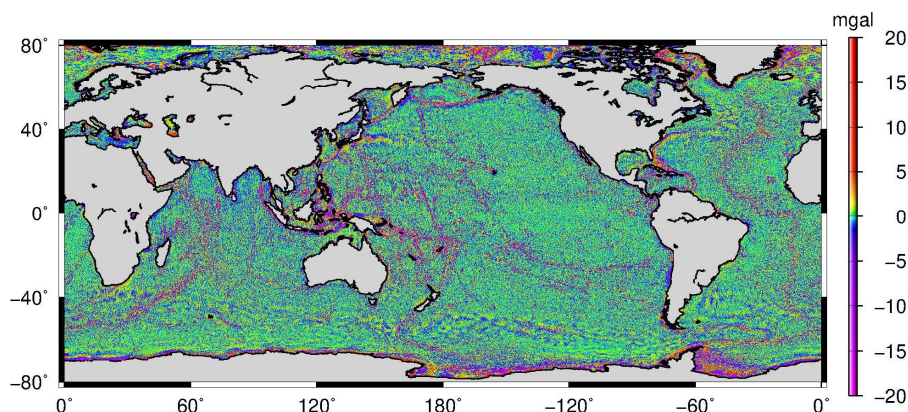
455 Due to being in the early stages of satellite altimetry, Geosat and ERS-1 may suffer from  
456 inherent ranging errors and orbit determination issues that could lead to degraded data quality.  
457 Considering the vast amount of observations accumulated in recent decades, it is worthwhile to  
458 consider removing low-quality and redundant data. For Geosat, its extensive accumulated data  
459 volume and dense coverage in high-latitude region, coupled with its unique 108° orbital inclination,  
460 make it a distinct group of observations with independent direction. Therefore, we have chosen to  
461 temporarily retain Geosat data in the NSOAS24 model construction. ERS-1 has also accumulated a  
462 significant amount of data. However, within the same directional group in Table 2, SARAL/AltiKa  
463 and Envisat share a substantial number of grid points that overlap completely with ERS-1  
464 (accounting for 30.7% of overlap). During the gridding process, these overlapping data points were  
465 stacked. In other words, 30.7% of ERS-1's data can be entirely replaced by higher-precision data  
466 from SARAL/AltiKa and Envisat. From the perspective of controlling points, it is noteworthy that  
467 control points in all directions exhibit a duplication rate exceeding 95%. Therefore, with adequate  
468 data coverage, multidirectional and high-quality precise slope data are required. Considering the  
469 previously identified poor performance and high replaceability, ERS-1 data has been ultimately  
470 removed in NSOAS24 model construction.

471 **4.4 Gravity anomaly inversion procedure**

472 Based on the DOV components at grid points, the residual gravity anomalies were calculated  
473 using the FFT method according to the Laplace Equation derived relationship, and the results were  
474 shown in Figure 14. Finally, a global marine gravity model over a range of 80°S-80°N with a 1'×1'  
475 grid interval, named NSOAS24, was constructed after restoring the removed reference model, as

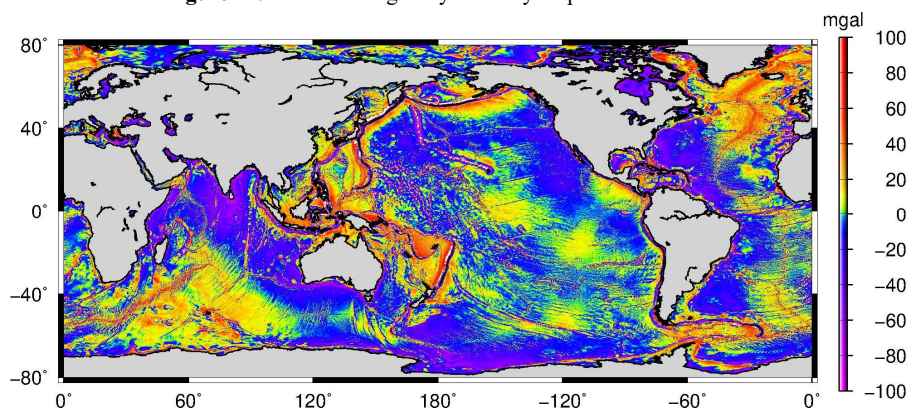


476 shown in Figure 15.



477  
478

**Figure 14.** The residual gravity anomaly map of NSOAS24



479  
480

**Figure 15.** The gravity anomaly map of NSOAS24

## 481 **5 Gravity anomaly results**

### 482 **5.1 Comparison with V32.1 and DTU21**

483 Firstly, the reliability of NSOAS24 was validated using altimetry-derived models, e.g., DTU21  
484 and V32.1, with statistical results summarized in Table 5. In Area 1 with relatively complex seafloor  
485 terrains, which includes the Mariana Trench, seamount chains, and numerous nearshore areas,  
486 NSOAS24 shows improvements of 0.6 mGal and 1.2 mGal over its predecessor (NSOAS22),  
487 compared to DTU21 and V32.1, respectively. In the predominantly open sea Area 2, NSOAS24  
488 demonstrates enhancements of 0.5 mGal and 0.7 mGal over NSOAS22, compared to DTU21 and  
489 V32.1, separately. Area 3 shows a 0.3 mGal improvement for NSOAS24 over NSOAS22, compared  
490 to DTU21, and a 1.0 mGal improvement compared to V32.1.





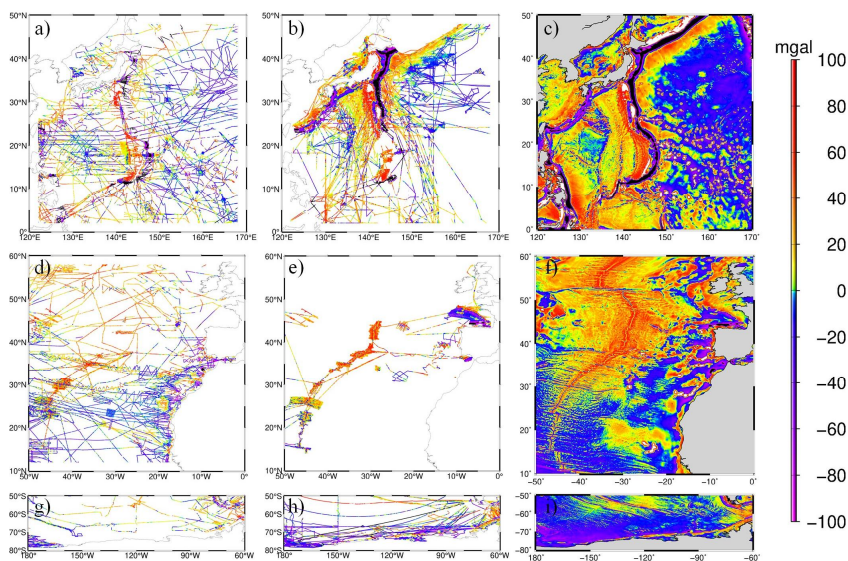
491 **Table 5.** Statistics of NSOAS24 and its predecessor against DTU21 and V32.1 (unit: mGal)

Area	Model	Max	Min	Mean	STD
1	NSOAS22-DTU21	202.64	-196.75	-0.09	3.56
	NSOAS24-DUT21	238.23	-255.97	0.02	2.93
	NSOAS22-V32.1	167.32	-196.69	-0.13	3.15
	NSOAS24-V32.1	91.36	-243.28	-0.03	1.97
2	NSOAS22-DTU21	71.89	-163.61	-0.07	1.96
	NSOAS24-DUT21	104.50	-72.45	-0.03	1.46
	NSOAS22-V32.1	63.64	-159.40	-0.05	1.95
	NSOAS24-V32.1	109.01	-101.60	-0.01	1.23
3	NSOAS22-DTU21	90.40	-167.89	0.02	6.32
	NSOAS24-DUT21	195.52	-223.07	0.02	6.01
	NSOAS22-V32.1	329.41	-195.06	-0.08	4.63
	NSOAS24-V32.1	305.43	-188.36	-0.08	3.61

492 **5.2 Comparison with shipborne gravity data**

493 The distribution of shipborne data and corresponding gravity anomalies of NSOAS24 model  
 494 in three experimental areas are illustrated in Figure 16. In Area 1, NCEI data show relatively even  
 495 distribution, while JAMTEC data are concentrated near Japan with dense nearshore coverage. In  
 496 Area 2, NCEI data are involved within entire region, while FOCD and SHOM data are primarily  
 497 concentrated along the Mid-Atlantic Ridge. In Area 3, NCEI data are sparse, with fewer  
 498 observations, whereas MGDS data are more evenly distributed and voluminous. Statistical  
 499 comparisons are presented in Table 6. The analysis highlights that NSOAS24 significantly improves  
 500 accuracy compared to NSOAS22. Furthermore, NSOAS24 demonstrates accuracy comparable to  
 501 DTU21 and V32.1, and outperforms V32.1 in the high-latitude polar regions.

502 Finally, these models were validated using worldwide distributed shipborne data. The accuracy  
 503 of each model was assessed using two sets of shipborne data: the early NCEI dataset and the recent  
 504 high-quality dataset from JAMTEC, MGDS, FOCD, and SHOM. The results are summarized in  
 505 Table 7. In general, NSOAS24 demonstrates accuracy comparable to DTU21 and V32.1. Compared  
 506 to its predecessor, NSOAS24 shows a steady improvement in accuracy, with a declination of ~0.7  
 507 mGal in standard deviations when compared with recent non-NCEI shipborne data.



508

509

510

511

**Figure 16.** Distribution of NCEI and non-NCEI shipborne data, and recovered gravity anomalies

**Table 6.** Statistics on differences between altimeter-derived models and shipborne gravity data (unit: mGal)

Area	Model	Ship-borne data	Max	Min	Mean	STD	Ship-borne data	Max	Min	Mean	STD
1	NSOAS22		55.82	-45.38	-0.52	6.14		40.20	-42.62	0.97	5.18
	NSOAS24		37.07	-41.06	-0.68	5.60		35.15	-42.88	1.12	4.97
	DTU21	NCEI	36.09	-42.72	-0.72	5.12	JAMTEC	24.90	-26.20	0.56	4.37
	V32.1		54.68	-68.25	-0.68	5.07		57.91	-66.35	0.74	4.99
	EGM2008		15.00	-15.00	-0.61	5.70		15.00	-15.00	0.52	4.93
2	NSOAS22		33.02	-29.06	3.07	7.28		29.74	-31.69	2.93	6.95
	NSOAS24		27.35	-27.61	3.24	7.21		26.67	-25.17	3.17	6.60
	DTU21	NCEI	23.96	-22.73	3.16	7.17	FOCD	22.14	-18.70	3.14	6.48
	V32.1		36.84	-26.69	3.19	7.19	SHOM	29.45	-19.20	3.16	6.45
	EGM2008		15.00	15.00	2.87	7.13		15.00	15.00	2.78	6.74
3	NSOAS22		35.16	-46.12	2.54	6.40		39.72	-43.68	-0.10	6.18
	NSOAS24		189.58	-38.36	2.56	6.21		44.94	-68.45	-0.09	5.92
	DTU21	NCEI	23.28	-41.36	3.20	5.79	MGDS	44.68	-58.59	0.16	5.83
	V32.1		279.57	-142.13	2.64	7.79		235.69	-114.62	0.41	8.68
	EGM2008		15.00	15.00	2.42	6.28		15.00	15.00	-0.08	6.19

512

**Table 7.** Verifications with globally distributed shipborne data (unit: mGal)

Model	Ship-borne data and number(pcs)	Max	Min	Mean	STD	Ship-borne data and number(pcs)	Max	Min	Mean	STD
NSOAS22		56.39	-67.77	1.48	6.64	JAMTEC	48.46	-48.02	1.00	5.64
NSOAS24		183.63	-134.00	1.49	6.33	MGDS	48.08	-156.23	1.01	4.95
DTU21	NCEI	46.37	-57.59	1.34	6.20	FOCD	44.68	-81.73	0.71	4.71
V32.1	(10740231)	279.59	-193.98	1.41	6.40	SHOM	297.00	-114.62	0.86	5.53
EGM2008		15.00	-15.00	1.24	6.33	(33522351)	15.00	-15.00	0.67	5.20

513

## 6 Conclusions

514

Based on our global marine gravity model construction experience in NSOAS22, we initially



515 optimized the dataset by incorporating recent observations and excluding highly substitutable ERS-  
516 1 data. Then, multi-satellite datasets were uniformly prepared for constructing a new global marine  
517 gravity model. During the processing, satellites with different orbital inclinations were firstly  
518 grouped into 5 categories. For multi-cycle ERM data, they were appended to the same data file in a  
519 way that preserves the temporal continuity of the data without disruption. Secondly, raw waveforms  
520 were retracked using the two-step weighted least-square retracker, and high-rate observations along  
521 profiles were uniformly resampled into 5 Hz to enhance the density of available measurements.  
522 Thirdly, pre-processing and slope editing were applied to the SSH measurement data to remove  
523 outliers, and the Parks–McClellan filter was used to constrain the amplified high-frequency noise  
524 during the differencing procedure. Fourthly, the residual along-track DOV was calculated from  
525 slopes by dividing by corresponding along-track velocities and introducing EGM2008 as a reference  
526 model. Fifthly, gridded DOV were determined from along-track DOV by the Green's function  
527 method. Finally, a global marine gravity model was constructed after FFT and corresponding inverse  
528 transform, restoring the removed reference model.

529 Comparing with the predecessor NSOAS22, several optimizations and improvements were  
530 implemented during the entire processing procedures for building NSOAS24. (1) Employing block-  
531 based input and output, calculations were executed with a 64\*64 grid input and output the central  
532 32\*32 grid. This improvement effectively resolved poor accuracy issues at boundaries and  
533 eliminated discontinuities between adjacent regions. (2) Utilizing the Green's function method to  
534 solve the DOV components, we increased the step size from 2 to 3 for selecting grid points as control  
535 points for iteration. This optimization aimed to enhance computational efficiency, reduce matrix  
536 complexity, and achieve noise smoothing effects. (3) We implemented specialized processing in  
537 coastal regions by incorporating a continental mask. The identified land points were assigned a  
538 default value with huge uncertainty to mitigate their weight. This approach effectively suppressed  
539 boundary effects near coastlines and controlled data divergence.

540 The new NSOAS24 model was firstly validated with well-known altimetry derived models.  
541 Comparisons were made in three experimental areas (Low-latitude, Mariana Trench area; mid-  
542 latitude: Mid-Atlantic Ridge area. High-latitude, Antarctic area) against the DTU21 and V32.1.  
543 Compared to the predecessor NSOAS22, NSOAS24 showed improvements of 0.6 mGal, 0.5 mGal,



544 0.3 mGal, and 1.2 mGal, 0.7 mGal, 1.0 mGal, respectively. Next, we utilized two sets of shipborne  
545 data to verify the new model: the earlier NCEI dataset and the recent non-NCEI dataset collected  
546 from JAMTEC, MGDS, FOCD, SHOM. NSOAS24 also demonstrated a steady improvement in  
547 accuracy compared to NSOAS22. Finally, on a global scale, we validated NSOAS24 (6.33 mGal  
548 and 4.95 mGal) using the NCEI dataset and the combined dataset from JAMTEC, MGDS, FOCD,  
549 and SHOM (6.20 mGal and 4.71 mGal for DTU21; 6.40 mGal and 5.53 mGal for V32.1).  
550 NSOAS24's accuracy was comparable to DTU21 and V32.1, with a notable improvement over  
551 NSOAS22 (6.64 mGal and 5.64 mGal). It is worth mentioning that NSOAS24 showed a decline in  
552 standard deviations of around 0.7 mGal compared to NSOAS22 when comparing with non-NCEI  
553 data. In conclusion, validations with both altimetry-derived models and shipborne data proved the  
554 effectiveness of optimizations and reliability of the NSOAS24 model.

#### 555 **Author contributions**

556 SZ and RZ contributed to the development of the global marine gravity anomaly model. Writing of  
557 the original draft was undertaken by XC and SZ, and YJ contributed to review and editing. All  
558 authors checked and gave related comments for this work.

#### 559 **Data availability**

560 The global marine gravity anomaly model, NSOAS24, is available at the ZENODO repository,  
561 <https://doi.org/10.5281/zenodo.12730119> (Zhang et al., 2024). The dataset includes global marine  
562 gravity anomalies in NetCDF file format.

#### 563 **Competing interests**

564 The contact author has declared that none of the authors has any competing interests.

#### 565 **Acknowledgements**

566 We are very grateful to AVISO for providing the altimeter data, and NCEI, JAMTEC, MGDS,  
567 FOCD, SHOM for providing shipborne gravity. We are also thankful to SIO and DTU for their  
568 published altimetry derived gravity models. Thanks to ICGEM for providing earth gravity models.



569 **Financial support**

570 This study was supported by the National Nature Science Foundation of China, grant number  
571 421932513.

572 **References**

573 Andersen O. B., Knudsen P.: The DTU17 global marine gravity field: First validation results. In:  
574 International Association of Geodesy Symposia, Springer: Berlin/Heidelberg, Germany,  
575 [https://doi.org/10.1007/1345\\_2019\\_65](https://doi.org/10.1007/1345_2019_65), 2019.

576 Andersen, O. B., Rose, S. K., Abulaitijiang, A., Zhang, S., & Fleury, S.: The DTU21 global mean  
577 sea surface and first evaluation, Earth System Science Data Discussions., 1-19.  
578 <https://doi.org/10.5194/essd-15-4065-2023>, 2023.

579 Brammer, R. F., Sailor, R. V.: Preliminary estimates of the resolution capability of the Seasat radar  
580 altimeter, Geophysical Research Letters., 7(3), 193-196,  
581 <https://doi.org/10.1029/GL007i003p00193>, 1980.

582 Chen, X., Kong, X., Zhou, R., Zhang, S.: Fusion of altimetry-derived model and ship-borne data in  
583 preparation of high-resolution marine gravity determination, Geophysical Journal  
584 International., 236(3):1262–1274, <https://doi.org/10.1093/gji/ggad471>, 2024.

585 Fu, L.-L. and Cazenave, A.: Satellite altimetry and earth sciences: a handbook of techniques and  
586 applications, Academic, San Diego, United States, ISBN 978-0-12-269545-2, 493 pp., 2001.

587 Guo, J., Luo, H., Zhu, C., Ji, H., Li, G., Liu, X.: Accuracy comparison of marine gravity derived  
588 from HY-2A/GM and CryoSat-2 altimetry data: a case study in the Gulf of Mexico,  
589 Geophysical Journal International., 230(2):1267–1279, <https://doi.org/10.1093/gji/ggac114>,  
590 2022b.

591 Hao, R., Wan, X., Annan, R.F.: Enhanced Short-Wavelength Marine Gravity Anomaly Using Depth  
592 Data, IEEE Transactions on Geoscience and Remote Sensing., 61, 1-9,  
593 <https://doi.org/10.1109/TGRS.2023.4242967>, 2023.

594 Li, Q., Bao, L., Wang, Y.: Accuracy Evaluation of Altimeter-Derived Gravity Field Models in  
595 Offshore and Coastal Regions of China. Front. Earth Sci., 9, 722019,  
596 <https://doi.org/10.3389/feart.2021.722019>, 2021.



- 597 Mohamed, A., Ghany, R.A.E., Rabah, M., Zaki, A.: Comparison of recently released satellite  
598 altimetric gravity models with shipborne gravity over the Red Sea. *Egypt. J. Remote Sens.*  
599 *Space Sci.*, 25, 579–592, <https://doi.org/10.1016/j.ejrs.2022.03.016>, 2022.
- 600 Pavlis, N.K., Holmes, S.A., Kenyon, S.C., Factor, J.K.: The development and evaluation of the Earth  
601 Gravitational Model 2008 (EGM2008), *J. Geophys. Res.*, V117, B04406,  
602 <https://doi.org/10.1029/2011JB008916>, 2012.
- 603 Sandwell, D.T., Harper, H., Tozer, B., Smith, W.H.F.: Gravity field recovery from geodetic altimeter  
604 missions. *Adv. Space Res.*, 68, 1059–1072, <https://doi.org/10.1016/j.asr.2019.09.011>, 2019.
- 605 Sandwell, D.T., Smith, W.H.: Marine gravity anomaly from Geosat and ERS 1 satellite altimetry.,  
606 *Journal of Geophysical Research:Solid Earth.*, 102(B5): 10039-10054,  
607 <https://doi.org/10.1029/96JB03223>, 1997.
- 608 Stammer, D. and Cazenave, A.: *Satellite altimetry over oceans and land surfaces*, CRC Press, Boca  
609 Raton, <https://doi.org/10.1201/9781315151779>, 2017.
- 610 Wan, X., Annan, R.F., Jin, S., Gong, X.: Vertical deflections and gravity disturbances derived from  
611 HY-2A Data, *Remote Sens.*, 12(14), 2287, <https://doi.org/10.3390/rs12142287>, 2020.
- 612 Wan, X., Hao, R., Jia, Y., Wu, X., Wang, Y., Feng, L.: Global marine gravity anomalies from multi-  
613 satellite altimeter data, *Earth Planets Space.*, 74, 165, [https://doi.org/10.1186/s40623-022-](https://doi.org/10.1186/s40623-022-01720-4)  
614 [01720-4](https://doi.org/10.1186/s40623-022-01720-4), 2022.
- 615 Wessel, P., Bercovici, D.: *Interpolation with Splines in Tension: A Green's Function Approach*,  
616 *Mathematical Geology.*, 30, 77–93, <https://doi.org/10.1023/A:1021713421882>, 1988.
- 617 Zhang, S., Andersen, O.B., Kong, X., Li, H.: Inversion and validation of improved marine gravity  
618 field recovery in South China Sea by incorporating HY-2A altimeter waveform data, *Remote*  
619 *Sensing.*, 12(5):802, <https://doi.org/10.3390/rs12050802>, 2020.
- 620 Zhang, S., Chen, X., Zhou, R., Jia, Y.: A new global marine gravity model NSOAS24 derived  
621 from multi-satellite sea surface slopes, Zenodo [Data set],  
622 <https://doi.org/10.5281/zenodo.12730119>, 2024.
- 623 Zhang, S., Sandwell, D.T.: Retracking of SARAL/AltiKa radar altimetry waveforms for optimal  
624 gravity field recovery, *Marine Geodesy.*, 40(1), 40–56,  
625 <https://doi.org/10.1080/01490419.2016.1265032>, 2017.



- 626 Zhang, S., Zhou, R., Jia, Y., Jin, T., Kong, X.: Performance of HaiYang-2 Altimetric Data in Marine  
627 Gravity Research and a New Global Marine Gravity Model NSOAS22, *Remote Sens.*, 14, 4322,  
628 <https://doi.org/10.3390/rs14174322>, 2022.
- 629 Zhu, C., Guo, J., Gao, J., Liu, X., Hwang, C., Yu, S., Yuan, J., Ji, B., and Guan, B.: Marine gravity  
630 determined from multi-satellite GM/ERM altimeter data over the South China Sea: SCSGA  
631 V1.0, *J. Geodesy*, 94, 50, <https://doi.org/10.1007/s00190-020-01378-4>, 2020.
- 632 Zhu, C., Guo, J., Yuan, J., Li, Z., Liu, X., & Gao, J.: SDUST2021GRA: Global marine gravity  
633 anomaly model recovered from Ka-band and Ku-band satellite altimeter data, *Earth System  
634 Science Data.*, 1-23, <https://doi.org/10.5194/essd-14-4589-2022>, 2022.